Inverse modeling of a single ring infiltration experiment: a key for analyzing unsaturated hydraulic properties of soils?

Michal Kuraz[a], Lukas Jacka[a], Johanna Ruth Blöcher[a], Matej Leps[b]

[a]*Czech University of Life Sciences Prague, Faculty of Environmental Sciences, Department of Water Resources and Environmental Modeling*
[b]*Czech Technical University in Prague, Faculty of Civil Engineering, Department of Mechanics*

Abstract

This contribution evaluates a possibility of identification of soil hydraulic properties (SHP) from inverse modeling of a single ring (hereafter SR) infiltration experiment. The SR experiment is a standard and robust dynamic field experiment. The steady state part of this experiment is traditionally used for an identification of saturated hydraulic conductivity. In this contribution, we explore the possibility of extending an applicability of this experiment for evaluating the unsaturated hydraulic parameters from an unsteady part of this experiment using inverse analyses of the governing flow motion equation.

The problem of SR infiltration is governed by qualisilinear Richards equation. We further present a methodology to avoid convergence issues with the nonlinear operator, originating from non-physical combinations of input parameters, which can be hard to avoid when automaticaly analyzing broad parameter space. With this methodology, we can answer (1) to what extent the well-known SR experiment is robust enough to provide a unique estimate of SHP parameters using the unsteady part of the infiltration experiment and (2) whether all parameters are vulnerable to non-uniqueness. We validated our methodology with synthetic infiltration benchmark problems for clay and sand, and applied on a real-world SR infiltration data. To evaluate non-uniqueness, local optima were identified and mapped using a modified genetic algorithm with niching, which is not possible with commonly used gradient methods.

Our results show the existence of multimodality in, both, the benchmark problems and the real-world problem. This is an important finding as local optima can be identified, which are not necessarily physical and also for systems that do not exhibit multimodal grain size distributions. The identified local optima were distinct and showed different retention and hydraulic conductivity curves. The most physical set of SHP could be identified with the knowledge of saturated water content, which makes it yet more obvious that expert knowledge is key in inverse modeling.

Keywords: soil hydraulic properties, inverse modeling, Richards equation, convergence issues, automatic calibration, computational issues in geosciences

1. Introduction

Soil hydraulic properties (hereafter SHP) are important for many hydrological models and engineering applications. The mountainous podzolic soil evaluated here is typical for the source areas of many major rivers in the Central European region. The top layer of the soil plays a key role in the rainfall-runoff process, because it is the top-soil that separates the rainfall into surface runoff and subsurface runoff.

Due to the rocks present and the dense root system of the covering vegetation, and due to the possible extension of the representative elementary volume, it is often impossible to collect undisturbed samples of top-soil for laboratory measurements in order to obtain the SHP parameters (Jačka et al., 2014). The SHP of the topsoil are therefore very difficult to measure directly (Fodor et al., 2011; Jačka et al., 2014).

In our study, the well-known single ring (hereafter SR) method was used to obtain experimental input data (cumulative infiltration) for inverse modeling. The SR infiltrometer is a widely accepted, simple, robust field method, which is able to measure the infiltration process, which affects the entire soil profile including the top-soil, and can sample a relatively large volume (depending on the diameter of the ring) (Cheng et al., 2011; Reynolds, 2008a). The SR infiltration experiment is an in situ experiment, which does not require soil samples to be collected, so the porous medium is kept relatively undisturbed. With the widely-used ring diameter of 30 cm, the affected porous media is far more representative than any soil sample we were able to collect. The top-soil can also be measured (with some alteration of the surface) using other well-known field infiltration methods, e.g. the tension infiltrometer or the well permeameter (Angulo-Jaramillo et al., 2000; Reynolds, 2008b).

The Richards equation (Richards, 1931) describes flow in variably saturated porous media. In order to model environmental processes and engineering applications with the Richards equation knowledge of the SHP is essential. SHP can be summarized by the soil water retention curve and soil hydraulic conductivity curve. In this contribution, the SHP are parametrized with the frequently used Mualem-van Genuchten model (van Genuchten, 1980). We refer to this model as REVG.

The identification of SHP from transient infiltration experiments has been a subject of numerous publications in past decades (Inoue et al., 2000; Lassabatère et al., 2006; Kohne et al., 2006; Xu et al., 2012; Bagarello et al., 2017; Younes et al., 2017). Inoue et al. (2000) reported a close correspondence between the SHP obtained from the inverse modeling of dynamic transient infiltration experiments with those obtained from steady-state laboratory experiments, where the uniqueness of the inverse model was preserved by considering the dynamically changing pressure head, water content and even tracer concentration.

The non-uniqueness of the REVG inverse model is already a very well-known issue, and has been described by a number of publications over the last decades (Kool et al., 1985; Mous, 1993; Hwang and Powers, 2003; Binley and Beven, 2003; Kowalsky et al., 2004; Nakhaei and Amiri, 2015; Kamali and Zand-Parsa, 2016; Peña-Sancho et al., 2017). Mous (1993) defined criteria for model identifiability based on the sensitivity matrix rank, however numerical computation of the sensitivity matrix, which is defined by the derivatives of the objective function,

often involves difficulties in managing truncation and round-off errors. Binley and Beven (2003) demonstrated on a real world case study of Sherwood Sandstone Aquifer that many different SHP parameters of macroscopic media can represent the layered unsaturated zone and provide acceptable simulations of the observed aquifer recharges. Mous (1993) explained that in case of the absence of water content data, the residual water content should be excluded from the identification to avoid non-uniqueness. However, Binley and Beven (2003) used a non-unique definition where both the unknown residual and saturated water content were considered. The definition of a unique inverse function for identification of macroscopic media was treated in (Zou et al., 2001), where the recommended approach was to assemble the objective function from transient data of the capillary pressure and from the steady state water content data.

A challenging issue is the treatment of the nonlinear operator of the Richards equation. Binley and Beven (2003) reported that 56% of the simulations were rejected during Monte Carlo simulations on a wide range of parameters, because of convergence problems. Their study did not mention explicitly why. We assume that these convergence issues originated from the nonlinear operator treatment.

The following questions arise:

- How can convergence issues be avoided, especially when the parameter range is wide?

- Is it possible to approximate the unsteady SR experiment using the REVG model, where the only unknown parameters represent the thin topsoil layer, by a unique set of parameters?

- If not, are all parameters vulnerable to non-uniqueness?

To answer these questions we employed a new calibration methodology.

1.1. Comment on system of units applied in this manuscript

Due to spatial and temporal scales of all model scenarios evaluated in this manuscript, instead of the base SI units we preferred to make use of *non-SI units accepted for use with the SI*. The length [L] will be always given in [cm], and the time [T] will be always given in [hrs].

2. Methodology

This section is divided into two parts. The first part, section 2.1, is focused on assembling the experimental data, which were later used as input for the inverse model. The site description, the reconstruction of the parameters of the SHP for the lower profiles, and the processing of the experimental data is given.

The second part of the methodology covers issues in the REVG inverse model. Section 2.2 derives governing equations and is given together with notes on the numerical stability of the REVG model for rotational symmetric problems. Section 2.3 discusses issues in creating the domain scheme and selecting appropriate boundary conditions, since it is not always easy to find an agreement between the mathematical model setup and physical
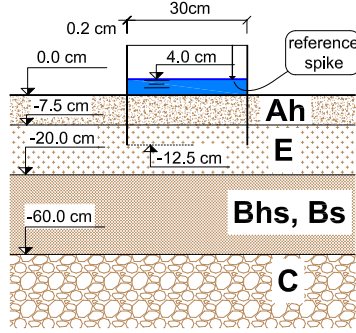
Figure 1: Scheme of the single ring infiltration experiment and the soil layers.

interpretation. Section 2.4.1 concludes with a description of the construction of the objective function, and the methodology of the automatic calibration.

2.1. Obtaining the input data for the inverse problem

2.1.1. Site description and assembling the experimental data

The study site is located in the Šumava National Park, and has been described in (Jačka et al., 2014). The location of the site in a map of Modrava 2 catchment is presented by Jačka et al. (2012). The soil profile is described by four different layers as seen on figure 1. The average groundwater table level can be roughly estimated at -280 cm below the surface. The soil hydraulic properties of the lower layers were identified by Guelph permeameter measurements (GP) with a methodology described by Jačka et al. (2014). Table 1 shows SHP parameters for spodic and eluvial horizons E, Bhs/BS and C below the top-soil calculated with the pedotransfer function implemented in Rosetta (Schaap et al., 2001) based on soil texture and the bulk density measurements.

Table 1: Soil hydraulic properties for the lower horizons.

horizon	GP experiment sites	θ_s [-]	α [cm^{-1}]	n [-]	K_s [cm.hrs^{-1}]	S_s [cm^{-1}]
E	28	0.46	0.046	1.741	1.584	0
Bhs + Bs	19	0.47	0.022	1.450	0.540	0
C	8	0.50	0.035	4.030	3.060	0

2.1.2. SR experimental setup

The experimental setup of the SR experiment was as follows. A steel ring 30 cm in inner diameter, 25 cm in length, and 2 mm in thickness was inserted into the soil to a depth of 12.5 cm, see figure 1. The depth of ponding was kept approximately at a constant level defined by a reference spike, which was placed 4 cm above the surface of the soil. The average experiment duration was 60 minutes.

A total of 22 SR experiments were conducted on the site. In order to eliminate noise from the experimental values, each SR experiment data set was smoothed with the Swartzendruber analytical model (Swartzendruber,

[84] 1987) of one-dimensional infiltration, which exhibited an excellent fitting quality, with a mean Nash-Sutcliffe
[85] model efficiency coefficient 0.9974. The Swartzendruber equation for cumulative infiltration states that

$$I(t) = \frac{c_0 \left(1 - \exp\left(-c_1 \sqrt{t}\right)\right)}{c_1} + c_2 t, \tag{1}$$

[87] where I is the cumulative infiltration [L], and $c_{0,1,2}$ are parameters. The Swartzendruber model can estimate
[88] 1D saturated conductivity and sorptivity of the soil. However, the model does not account for water moving
[89] horizontally and therefore overestimates the hydraulic conductivity and gives no information on water retention or
[90] unsaturated hydraulic conductivity and is therefore not sufficient. The Swartzendruber model was only considered
[91] as an exponential smoothing and interpolating function.

[92] A statistical description of the Swartzendruber parameters and their fitting quality is given in (Jačka et al.,
[93] 2016), see datasets collected on site 3. Representative mean values are as follows: $c_0 = 5.130$ cm.hrs$^{-0.5}$, $c_1 =$
[94] 1.13×10^{-1} [-], and $c_2 = 1.858$ cm.hrs^{-1}. The parameter set was used to compute the infiltration curve with (1)
[95] for the identification of the SHP in the top soil layer.

[96] *2.2. Mathematical model of the field infiltration experiment – governing equation*

[97] The field infiltration experiment is characterized by variably saturated conditions. The flux in porous media
[98] under variably saturated conditions can be expressed by the Darcy-Buckingham law (Buckingham, 1907)

$$\mathbf{q} = -\mathbf{K}(\theta)\nabla H, \tag{2}$$

[100] where $\mathbf{q}$ is the volumetric flux [L.T^{-1}], H is the total hydraulic head [L] defined as $H = h+z$, where h is the pressure
[101] head [L], z is the potential head [L], θ is the water content [-], and $\mathbf{K}(\theta)$ is the unsaturated hydraulic conductivity
[102] [L.T^{-1}]; in general it is a second order tensor. The relation $\theta(h)$ is referred to as the retention curve (van Genuchten,
[103] 1980).

[104] The geometry of the flow is inherently three-dimensional, but the domain dimension can be reduced by consid-
[105] ering the axisymmetric geometry. The law of mass conservation for incompressible flow in cylindric coordinates
[106] is expressed as (Bear, 1979).

$$-\frac{\partial V}{\partial t} = \frac{\partial q_r}{\partial r} + \frac{q_r}{r} + \frac{\partial q_\alpha}{\partial \alpha} + \frac{\partial q_z}{\partial z}, \tag{3}$$

[108] where V is the volume function [-], r is the radial coordinate, α is the angular coordinate, z is the vertical co-
[109] ordinate, and $q_{r,\alpha,z}$ is the volume flux [L.T^{-1}]. The ring infiltration experiment is characterized by rotational
[110] symmetric flow, so the angular derivative vanishes. Then the governing equation for variably saturated and rota-
[111] tional symmetric flow is obtained by substituting the flux in (3) by the Darcy-Buckingham law (2). Together with
[112] the consideration of linear elasticity (expressed by specific storage S_s) for a porous medium the variably saturated
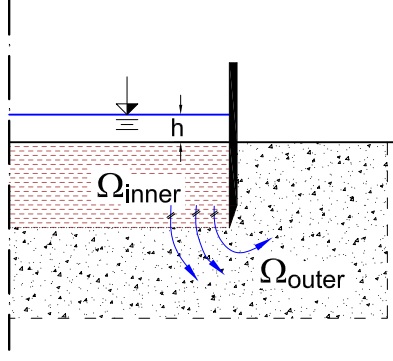
5

Figure 2: Scheme of the flow domain and the streamlines of infiltration experiment.

axisymmetric flow in isotropic media is governed by

$$\left(\frac{\mathrm{d}\theta}{\mathrm{d}h} + S_s \frac{\theta(h)}{\theta_s}\right)\frac{\partial h}{\partial t} = \frac{\partial K(h)\frac{\partial H}{\partial z}}{\partial z} + \frac{\partial K(h)\frac{\partial H}{\partial r}}{\partial r} + c(\mathbf{x})\frac{\partial H}{\partial r}, \tag{4}$$

where S_s is the specific storage [L^{-1}], θ_s is the saturated water content [-], $c(\mathbf{x})$ is the coefficient of the convection for r coordinate [T^{-1}], which is explained below, and the vector x is a vector of the spatial coordinates $\mathbf{x} = \binom{r}{z}$.

If we consider the model of the infiltration experiment depicted in figure 2 with the entire flow domain $\Omega = \Omega_{inner} \cup \Omega_{outer}$, where Ω_{outer} is the flow domain outside the infiltration ring and Ω_{inner} is the flow domain within the infiltration ring, exactly as depicted in figure 3. It is then apparent that the streamlines inside subdomain Ω_{inner} are parallel, but the streamlines outside the infiltration ring (inside Ω_{outer}) are only axisymmetric. The convection coefficient $c(\mathbf{x})$ is then defined as follows

$$c(\mathbf{x}) = \begin{cases} 0, & \forall \mathbf{x} \in \Omega_{inner} \\ \frac{1}{r}K(h), & \forall \mathbf{x} \in \Omega_{outer}. \end{cases} \tag{5}$$

Note that we should avoid using the coordinates, where $r = 0$.

2.3. Domain setup

2.3.1. Domain shape restrictions

It is well-known that sudden changes in domain shapes, spikes and discontinuities yield numerical difficulties (e.g. the Lipschitz boundary restrictions (Braess, 1997)). In order to avoid computational difficulties during the automatic calibration procedure the infiltration ring thickness was oversized to 2.5 cm. It is obvious that the real ring thickness is much smaller (in our case 2 mm), but using the real ring thickness yields possible numerical issues. It is expected, that oversizing the ring thickness does not significantly affect the fluxes through the top Dirichlet boundary, which is the only important part of the solution of (4) for our calibration process.
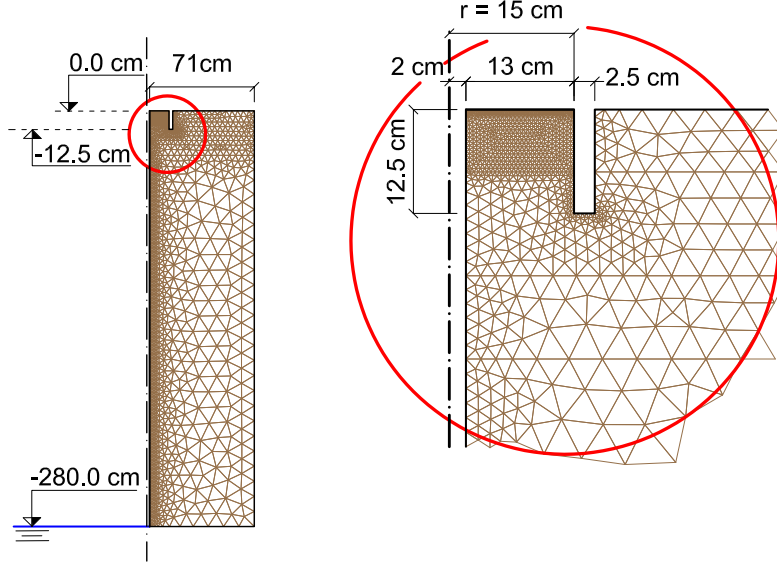
6

Figure 3: Scheme of the computational domain geometry and domain triangularization.

2.3.2. Stability restrictions of convection dominant problems

The equation (5) refers to coefficient of the first order derivative term in (4), and so the well known stability restrictions for the numerical solutions of the convection-diffusion problems appear here Christie et al. (1976). The Peclet number representing the numerical stability of convection-diffusion problems is defined as (Knobloch, 2008)

$$Pe = \frac{c\Delta x}{2D},\tag{6}$$

where c is the convection coefficient defined in (5), Δx is the discretization step, and D is the diffusion (for isotropic setup). Based on the definitions given above, equation (6) can be formulated as

$$Pe = \frac{\frac{1}{r}K(h)\Delta x}{2K(h)} = \frac{\Delta x}{2r}.\tag{7}$$

Since our mesh is triangular, Δx can be roughly assumed to be the greatest triangle altitude (since we assume some mesh quality properties). Then a sufficient distance from the axis of anisotropy is such that the Peclet number is sufficiently low. If we want to make our computation free of the well known spurious oscillations Christie et al. (1976); Roos et al. (1996), a sufficiently low Peclet number $Pe \leq 1$ is required. Therefore, the distance from the axis of anisotropy is given by the domain discretization step at the left hand side boundary. The selected discretization step at the left hand side boundary was assumed as $\Delta x = 2$ cm. The domain was therefore detached by 2 cm from the axis of anisotropy, and thus the Peclet number was 0.5 only.

7

2.3.3. Initial and boundary condition setup

The initial condition was assumed as a steady state solution of (4) with the boundary $\Gamma_1 \cup \Gamma_2$ assumed as a no-flow boundary – thus the entire domain Ω was considered to be in hydrostatic state. The initial condition states that

$$H(x) = -280.0 \text{ cm}; \quad \forall x \in \Omega, \tag{8}$$

and thus $\frac{\partial h}{\partial z} = -1$.

As discussed in 2.3.2 the left hand side boundary was located at $r = 2$ cm. The right hand side boundary was located at a distance $r = 73$ cm and 60 cm from the infiltration ring. The computational domain is depicted in figure 3 together with the discretization mesh. The location of the top boundary was natural – the soil surface. Inside the ring, a Dirichlet condition defines the ponding depth; outside the infiltration ring a Neumann condition defines the no-flow boundary. The depth and definition of the bottom boundary was more problematic. We consider following commonly used options:

- the no-flow boundary (Neumann)

- the free drainage boundary (Neumann)

- the groundwater level - zero pressure head (Dirichlet)

It is apparent that the wetting front originating from our infiltration experiment affects the soil column only to a certain depth. Defining the Neumann no-flow boundary at a sufficient depth would probably not have a significant effect on the cumulative flux at the top Dirichlet boundary. At the same time, the only physically acceptable location of the no-flow boundary is the groundwater table. The second option – the free drainage boundary – would be completely incorrect for any depth, because we consider the initial condition to represent a hydrostatic state, and so

$$\frac{\partial h}{\partial z}(x) = -1, \quad \forall x \in \Omega. \tag{9}$$

The free drainage boundary condition, which is defined as

$$\frac{\partial h}{\partial \mathbf{n}}(x) = 0, \quad \forall (x, t) \in \Gamma_{\text{free drainage}} \times [0, T). \tag{10}$$

is in a conflict with the initial condition (since the outer normal vector $\mathbf{n} = \left(\begin{smallmatrix} 0 \\ -1 \end{smallmatrix} \right)$), and produces extra computational costs. The computed fluxes produced at the bottom boundary in the beginning of the simulation with such a boundary setup, originates from the initial and boundary condition mismatch, and has no physical meaning.

Physically correct boundary conditions for the bottom boundary is either the Neumann no-flow boundary at the impermeable layer or Dirichlet boundary both at the groundwater table. We chose a constant Dirichlet boundary condition. The average depth of the groundwater table is approximately -280 cm below the surface, and we
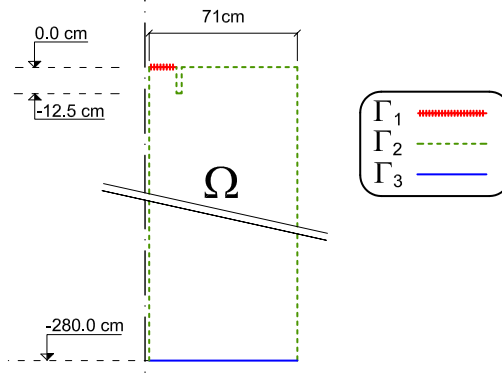
Figure 4: Scheme of the computational domain geometry and the domain boundaries.

assume that the water table remains constant during the experiment. With this particular setup the domain became extremely narrow and deep, see figure 3.

The locations of the domain boundaries are depicted in figure 4. The boundary conditions are specified as follows (with the reference level $z = 0$ located at the top boundary)

$$h(x,t) = 4 \text{ cm} \Rightarrow H(x,t) = 4 \text{ cm};$$

$$\forall (x,t) \in \Gamma_1 \times [0,T),$$

$$\frac{\partial H}{\partial \mathbf{n}} = 0; \ \forall (x,t) \in \Gamma_2 \times [0,T), \quad (11)$$

$$h(x,t) = 0 \text{ cm} \ \Rightarrow \ H(x,t) = -280.0 \text{ cm};$$

$$\forall (x,t) \in \Gamma_3 \times [0,T).$$

where T is the simulation end time [T], and $\mathbf{n}$ is the boundary normal vector.

2.4. Optimization

2.4.1. Objective function

The soil hydraulic parameters (SHP) of the top soil that will be identified were specified in section **??**. Since the parameters will be identified using a stochastic method, we have to introduce a range for each parameter. The ranges for the SHP are specified in table 2. These initial ranges are very broad, since we are trying to explore a possible non-uniqnuess of this inverse model.

Table 2: Ranges of SHP ($\mathbf{p}_{max}$ and $\mathbf{p}_{min}$) for identifying the SHP in the top-soil layer for *refinement level $r_f = 0$*. Note that the initial ranges are extremely broad especially for the saturated water content θ_s. This broad range was selected in order to explore the uniqnuess of the REVG inverse model of SR experiment even beyond the physically acceptable solutions.

θ_s [-]	α [cm^{-1}]	n [-]	K_s [cm.hrs^{-1}]	S_s [cm^{-1}]
$0.25 - 0.90$	$1 \times 10^{-4} - 5.000 \times 10^{-2}$	$1.05 - 4.5$	$0.300 - 300.0$	$0.0 - 0.1$

The objective function is defined in the following paragraph.

9

Let $\bar{I}(\mathbf{p}, t)$ be the cumulative infiltration obtained from solving the mathematical model (4) bounded by the initial and boundary conditions defined in section 2.3 for a certain vector of SHP parameters $\mathbf{p}$ considered as

$$\bar{I}(\mathbf{p}, t) = \frac{\int\limits_0^t \int\limits_{\Gamma_1} -K\frac{\partial H}{\partial \mathbf{n}}(t)\mathrm{d}\Gamma_1 \mathrm{d}t}{\int\limits_{\Gamma_1} \mathrm{d}\Gamma_1}. \tag{12}$$

Let $I(t)$ be the cumulative infiltration given by (1) with parameters given in section 2.1.2. Then the objective function was defined for three different criteria in order to avoid ill-posed objective function definition.

Both $\bar{I}(\mathbf{p}, t)$ and $I(t)$ are continuous functions. Note please, that this is not a standard configuration. The objective functions were then defined as follows:

I. First criterion Ψ_1 was defined as L_2 norm of the difference between the experimental and model data and thus

$$\Psi_1(\mathbf{p}) = \frac{\sqrt{\int\limits_0^{T_{end}} \left(\bar{I}(\mathbf{p}, t) - I(t)\right)^2 \mathrm{d}t}}{T_{end}}, \tag{13}$$

where T_{end} is the final simulation time $[T]$, which is indeed the root mean square error (RMSE) for continuous functions.

II. Second criterion was the L_∞ norm of the difference between the experimental and model data and thus

$$\Psi_2(\mathbf{p}) = \sup\left(\sqrt{\left(\bar{I}(\mathbf{p}, t) - I(t)\right)^2}\right), \quad t \in (0, T_{end}). \tag{14}$$

III. Third criterion was considered as the difference between the infiltration rates (final derivatives) between the model data and the experimental data

$$\Psi_3(\mathbf{p}) = \sqrt{\left(\frac{\mathrm{d}\bar{I}(\mathbf{p}, T_{end})}{\mathrm{d}t} - \frac{\mathrm{d}I(T_{end})}{\mathrm{d}t}\right)^2}. \tag{15}$$

We conducted multi-objective optimization. However, it is apparent that minimizing the objective function (13) also minimizes the objective functions (14) and (15). The aim of this multi-objective definition was to improve the conditioning of this inverse problem. If we only considered the objective function (13), then we were probably able to obtain the same solution as with this multi-objective definition with slower convergence of optimization procedure only (the selection of the optimization algorithm will be explained in the following section 2.4.2). This multi-objective function definition is based on our experience from previous attempts of inverse analysis of this infiltration problem.

2.4.2. Optimization algorithm

In this contribution we used the modified genetic algorithm GRADE (Ibrahimbegović et al., 2004; Kucerova, 2007) supported by niching method CERAF (Hrstka and Kucerova, 2004) enhancing the algorithm with memory and restarts. GRADE is a real-coded genetic algorithm combining the ideas of genetic operators: cross-over, mutation and selection taken from the standard genetic algorithm and differential operators taken from differential evolution. When GRADE converges, the current position of the optimization algorithm is marked as a local extreme and a forbidden area is built around it in order to forbid the optimization algorithm to fall into the same local extreme again. The main setting of the optimization procedure was as follows: the population of the genetic algorithm contains 30 independent solutions, the whole identification stops after 20.000 objective function evaluations and a local extreme was marked after 600 evaluations without any improvement.

GRADE project is capable for multi-objective definition for the objective function, which is achieved with so-called Average Ranking (AR) (Leps, 2007). It sums ranks of the objective functions instead of the objective functions' values. Therefore, no weights are needed, however, the Pareto-dominance is not preserved as described in Vitingerova (2010). An application of the AR algorithm to parameters identification can be found in Kuraz et al. (2010).

2.5. Numerical solution and computational issues

Equation (4) was implemented into the DRUtES library (Kuraz et al., 2008). It is an object-oriented library written in Fortran 2003/2008 standard for solving nonlinear coupled convection-diffusion-reaction type problems. The problem was approximated by the linear finite element method for spatial derivatives and Rothe's method for temporal derivatives. The nonlinear operator was treated with the Schwarz-Picard method – an adaptive domain decomposition (*dd*-adaptivity) – with the ability to activate and deactivate subregions of the computational domain sequentially (Kuraz et al., 2013a, 2014, 2015).

The domain was non-uniformly discretized by a triangular mesh. The smallest spatial step was considered for the top layers inside the infiltration ring, close to the Dirichlet boundary. The mesh is depicted on figure 3. The minimum spatial length was 0.5 cm, and the maximum spatial length was 20 cm. The domain was discretized with 2097 nodes and 3861 elements. The coarse mesh for the *dd*-adaptivity method was a uniform quadrilateral mesh with elements 17.75×28.0 cm, i.e. a total of 40 coarse elements and 55 nodes. The purpose of the coarse mesh is to organize the elements of the domain triangularization into so-called clusters, which form a basic unit for the adaptive domain decomposition used here for solving the nonlinear problem, details can be found in (Kuraz et al., 2015).

The spatial and temporal discretization of (4) leads to sequential solutions of systems of non-linear equations, see e.g. (Kuraz et al., 2013a). The system was linearized as discussed in Kuraz and Mayer (2013); Kuraz et al.

(2013b), and so the numerical solution requires an iterative solution of

$$\mathbf{A}(\mathbf{x}_l^k)\mathbf{x}_l^{k+1} = \mathbf{b}(\mathbf{x}_l^k), \tag{16}$$

where k denotes the iteration level, and l denotes the time level, until

$$\|\mathbf{x}_l^{k+1} - \mathbf{x}_l^k\|_2 < \varepsilon, \tag{17}$$

where ε is the desired iteration criterion. It is apparent that the number of required iterations depends on the ε criterion.

The method (16) degenerates into a kind of semiexplicit approximation if the error criterion ε was "infinitely huge" (in a theory it means taken from the extended real numbers, $\varepsilon \in \overline{\mathbb{R}}$, and assigned as $\varepsilon = +\infty$). This semiexplicit approximation is denoted as

$$\mathbf{A}(\mathbf{x}_{l-1})\mathbf{x}_l = \mathbf{b}(\mathbf{x}_{l-1}). \tag{18}$$

This semiexplicit method always requires just a single iteration. With a short time step the method converges to the exact solution. For inappropriate time steps, the method diverges from the exact solution faster than the method (16). Nonetheless, the method (18) is free of possible issues related to the convergence of the nonlinear operator.

3. Automatic calibration methodology

We address possible difficulties with convergence of the linearized discrete system (16) for certain combinations of SHP parameters during the automatic calibration, as discussed by Binley and Beven (2003). Moreover, we address the problem of multimodality when the initial range of SHP parameter is broad as in table 2. It is known that inaccurate approximation of the capacity term (time derivative term) yields inaccurate mass properties (Celia et al., 1990) and are aware of the possible impact of spatial and temporal discretization on the identified SHP values.

Following the concerns about effects of the numerical treatment on the identified SHP, we propose an automatic calibration methodology depicted in figure 5. Details are given in the following algorithm scheme. In brief, the proposed method uses less accurate, but fast and convergence-issue-free numerical technique, to identify (several) promising parameter regions. To avoid the influence of the numerical solver setup, the SHP estimate is consequently updated in each parameter region with an improved numerical treatment of the Richards equation solver. It is presumed that the inverse model solution is non-unique on the initial broad parameter range, but unimodal on the narrow region(s), which are subsequently investigated.

Let us define the following nomenclature:

12

---

r_f – "refinement level", the problem is treated with different spatial and temporal discretization setups, each setup is denoted by value of r_f index,

i_e – local extreme index,

$\mathbf{p}$ – vector of SHP parameters, vector contains the values of α, n, θ_s, K_s, S_s,

$\mathbf{p}_{max,min}^{r_f}$ – maximal, resp. minimal values of SHP parameters defining a parameter range for a certain refinement level r_f,

$\mathbf{p}_{max,min}^{i_e,r_f}$ – maximal, resp. minimal values of SHP parameters defining a parameter range for a certain refinement level r_f in a certain vicinity of a local extreme i_e,

$\Delta(\mathbf{x})$ – spatial discretization (mesh density, mesh is non-uniform).

The calibration algorithm is described as follows:

I. **Do** initial calibration with semiexplicit treatment of (16) ($\varepsilon \rightsquigarrow +\infty$), r_f=0, vectors $\mathbf{p}_{max,min}^{r_f}$ are taken from table 2.

II. **Create** sequence of vectors $\mathbf{p}_{r_f}^{i_e}$.

III. **If** the problem is multimodal

- **then** $i_e > 1$,
- **else** $i_e = 1$.

IV. **Do validation:**

(a) **select** local extremes with good fitting qualities,

(b) **increase** $r_f = r_f + 1$ as follows

$$
\begin{aligned}
\Delta(\mathbf{x})^{r_f} &= \frac{\Delta(\mathbf{x})^{r_f-1}}{2}, \\
\varepsilon^{r_f} &= 10^{-3} \text{ cm} \quad \text{if } r_f = 1, \\
\text{else} \quad \varepsilon^{r_f} &= \frac{\varepsilon^{r_f-1}}{10}, \\
t_{init}^{r_f} &= \frac{t_{init}^{r_f-1}}{10} \text{ hrs.}
\end{aligned}
\tag{19}
$$

13
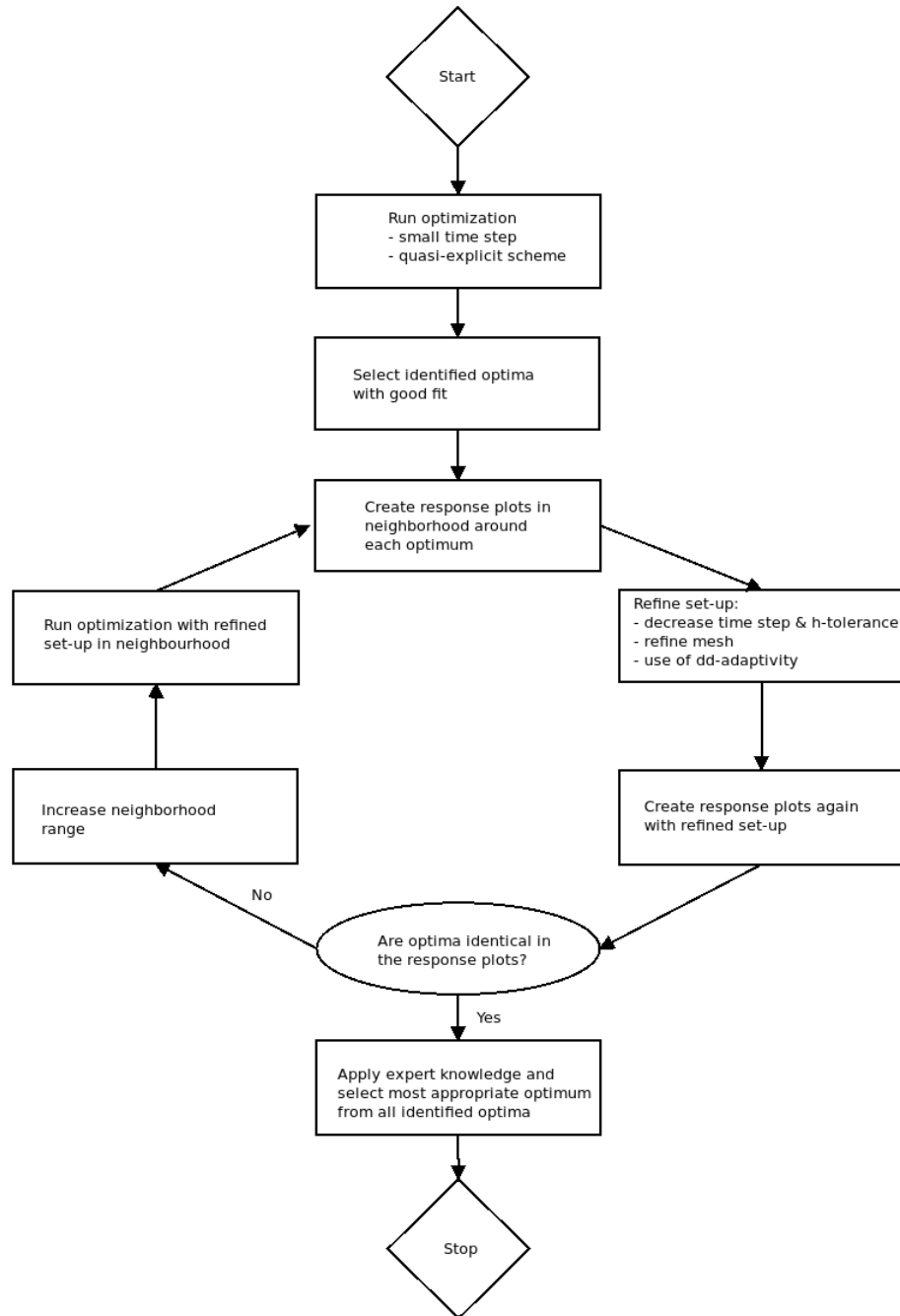
Figure 5: The proposed methodology for the automatic calibration avoiding effects of numerical treatment for the identified SHP values.

(c) **create** a response plot of (13) for current r_f and $r_f - 1$ in the neighborhood defined as

$$\mathbf{p}^{i_e,r_f}_{max} = 1.20\mathbf{p}^{i_e},$$

$$\mathbf{p}^{i_e,r_f}_{min} = 0.70\mathbf{p}^{i_e}. \tag{20}$$

(d) **Validation methodology:**

i. Visually **inspect** response plots for the selected local extreme i_e created with discretization r_f and $r_f - 1$.

ii. **If** the response plots differ significantly,

- **then redefine** the parameter range as specified in (20), **return** to **II .**, new sets of vectors $\mathbf{p}^{i_e}_{r_f}$ will be generated (only global extreme accepted at this stage, i_e points to the original local extreme), **proceed new validation**.

- **else exit** the calibration process.

4. Results and discussion

This section begins with a simple synthetic problem with known exact solution, which is given here to test the multimodality of this class of Richards equation inverse model, to provide a support for the methodology given in section 3. Later, we continue in section 4.2 with presenting our real world problem example, where we present our parameter estimate for the top soil organic horizon, obtained from the methodological approach explained above in 3.

4.1. Synthetic problem

The purpose of this benchmark example was to demonstrate, whether this class of problem – identification of SHP parameters from cumulative flux measured at Dirichlet boundary – can be affected by multimodality.

For simplicity only a one-dimensional Richards equation problem was considered here. Dirichlet boundary conditions were presumed for both boundaries. The model setup state as follows. Computational domain was $\Omega = (0, 100\,cm)$, and the boundary and initial conditions stated as follows

$$h(x,t) = 0\,cm, \quad \forall (x,t) \in \Gamma_{bot} \times t \in [0, T_{end})$$

$$h(x,t) = 0\,cm, \quad \forall (x,t) \in \Gamma_{top} \times t \in [0, T_{end}) \tag{21}$$

$$H(x,t_0) = 0\,cm, \quad \forall x \in \Omega,$$

where $\Gamma_{bot} = 0.0$ cm, $\Gamma_{top} = 100.0$ cm, and $T_{end} = 10^{-1}$ hrs. Two distinguished soil types were considered here – clay loam and sand, the parameters were obtained from (van Genuchten et al., 2009).

15

Table 3: Results of the synthetic problem. The grey highlighted rows refer to the physically acceptable solution of this benchmark inverse problem, and the red highlighted rows contain the exact solution of this inverse problem.

			parameters				RMSE error
			α [cm^{-1}]	n [-]	θ_s [-]	K_s [cm.hrs^{-1}]	
clay loam	exact solution		0.019	1.31	0.41	6.24	
	identified solutions	1	0.020	1.321	0.395	6.226	4.787×10^{-2}
		2	0.012	1.050	0.250	7.011	2.830×10^{-1}
		3	1.280×10^{-4}	1.146	0.900	94.904	3.724×10^{-1}
sand	exact solution		0.145	2.68	0.43	29.7	
	identified solutions	1	0.039	1.050	0.250	35.563	2.978×10^{-2}
		2	0.026	1.087	0.587	37.877	2.406×10^{-2}
		3	0.154	2.654	0.460	30.145	2.199×10^{-2}

The computational domain Ω was uniformly discretized with Δx=0.5 cm, the initial time step was Δt=10^{-7} hrs, and the error criterion from (17) for solving the nonlinear system (16) was ε=10^{-3} cm.

The reference solutions both for sand and gravel media were obtained from cumulative flux over the top Dirichlet boundary Γ_{top}.

For the given reference solutions the inverse modeling algorithm described in section 2.4.2 was employed for searching the original SHP parameters in broad ranges given in table 2. In order to avoid effects of numerical treatment of the Richards equation, the numerical solver had exactly the same configuration as the one used for the reference solution.

Results of the synthetic problem are given in table 3. For these two different soil types involved the inverse modeling algorithm has found several local optima, and the low value of an objective function doesn't necessarily point to the correct solution. Thus the problem is multi-modal. Several distinct SHP parameter sets can lead to acceptable solutions. However, the most distinct SHP parameter is the saturated water content θ_s. It turns out that an expert knowledge is required here, to select an acceptable solution of this inverse problem.

4.2. Real-world problem

We found multiple optima for the real-world problem. The local extremes for the refinement level $r_f = 0$ are given in table 5, where the gray lines refer to local extremes with bad fitting properties (extremes 1-5), the local extremes 6-8 refer to inverse model solutions with good fitting properties. The results were visually inspected. An example of bad fitting dataset is depicted on figure 6 - left, and the example of the good fitting dataset is depicted on figure 6 - right. Solution for each dataset is given in Appendix. Complete settings specifications for each r_f level involved here are given in table 4.

In the next step the refinement level was increased, new mesh was generated.

For the local extreme 6, the refined numerical treatment $r_f = 1$ has not affected the objective function, the figure 7 depicts two examples of the response plots – for the parameter α and n. The response plots of all parameters

16

Table 4: Settings for different r_f levels. Computer architecture 32-core Intel(R) Xeon(R) CPU E5-2630, bogomips 4801.67, objective functions were evaluated in parallel.

r_f level	Picard criterion ε [cm]	number of nodes	number of elements	initial Δt [hrs]	number of objective function evaluations	CPU time for objective function computation [min]
0	$\leadsto +\infty$	2097	3861	10^{-6}	40 000	3
1	10^{-3}	4503	8488	10^{-7}	1 000	20
2	10^{-4}	9637	18588	10^{-8}	1 000	60

Table 5: Identified local extremes of Pareto front during the first run of parameter search procedure.

no.	α [cm^{-1}]	n [-]	θ_s [-]	K_s [cm.hrs^{-1}]	S_s [cm^{-1}]	RMSE error (13) [cm] $r_f = 0$	RMSE error (13) [cm] $r_f = 1$
1	2.447×10^{-4}	2.450	0.25	2.500×10^{-2}	4.190×10^{-3}	3.632×10^{-1}	not computed
2	1.010×10^{-3}	2.651	0.271	1.092	2.879×10^{-2}	2.723×10^{1}	not computed
3	1.840×10^{-2}	2.098	0.353	1.092	1.845×10^{-4}	9.533×10^{-1}	not computed
4	1.570×10^{-3}	1.968	0.720	2.070	1.053×10^{-5}	2.290×10^{-1}	not computed
5	1.500×10^{-3}	1.586	0.720	1.093	7.641×10^{-5}	9.932	not computed
6	2.580×10^{-3}	2.152	0.401	1.095	0	1.993×10^{-2}	1.363×10^{-2}
7	3.802×10^{-3}	1.279	0.594	1.165	0	9.694×10^{-3}	8.630×10^{-2}
8	2.550×10^{-3}	1.384	0.254	1.119	1.922×10^{-4}	1.030×10^{-2}	4.152×10^{-2}
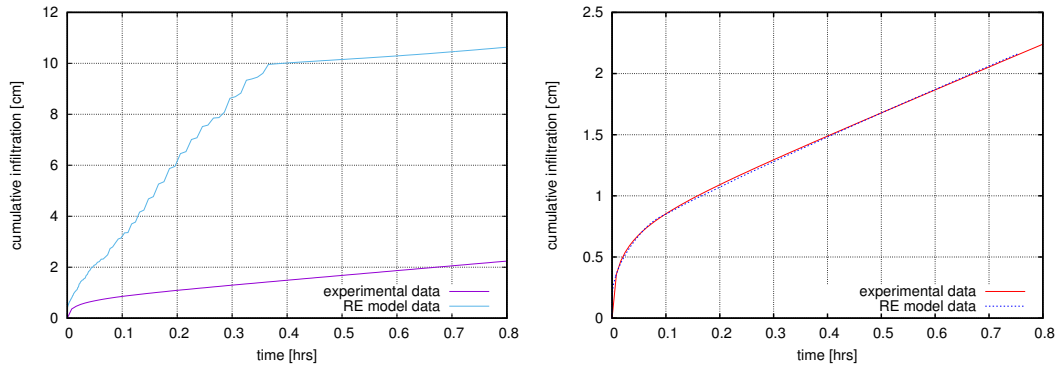
Figure 6: Left: Local extreme 2 – bad fitting properties, Right: Local extreme 5 – good fitting properties.
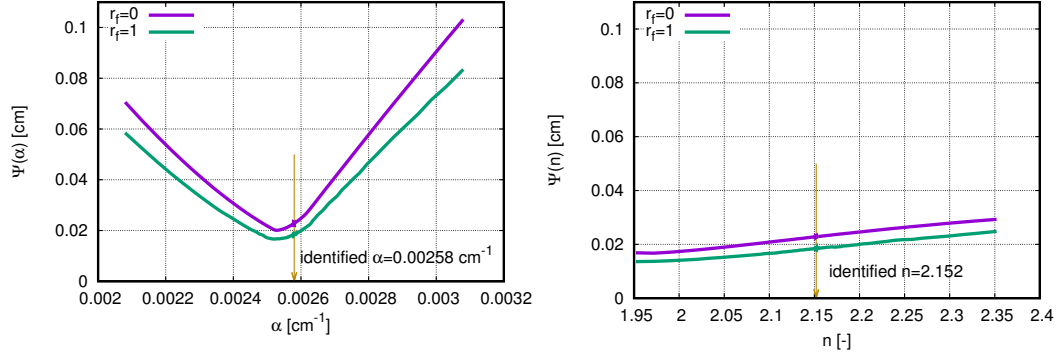
Figure 7: Response plots of the objective function (13) for the parameter α (left) and n (right) for extreme 6.
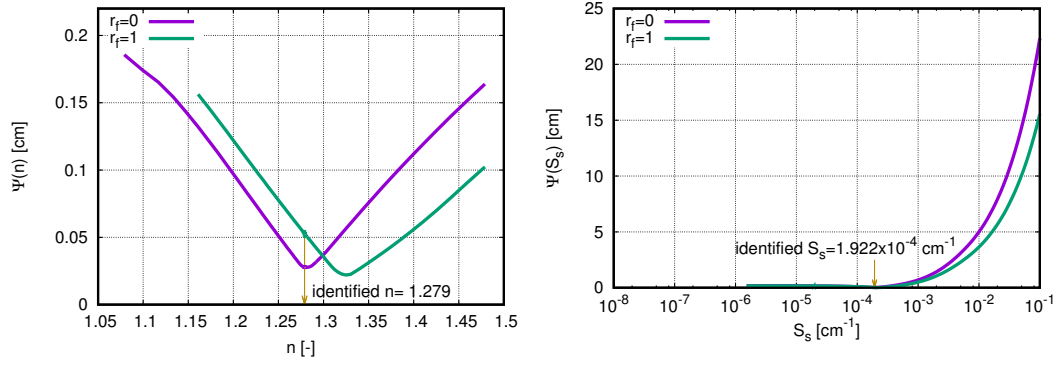
Figure 8: Response plots of the objective function (13) for the parameter n at extreme 7 (left) and S_s at extreme 8 (right)

.

are given in Appendix. The response for the α parameter (figure 7 - left) seems adequate, which was not the case of n parameter (figure 7 - right). It turns out that for this parameter set the objective function exhibits poor local sensitivity. However, this was not the case of the other local extremes, see figure 8 - left.

The local extreme 8 is characterized by nonzero specific storage S_s. However, if we look closer to the response plot 8 - right, it becomes apparent, that the specific storage should vanish even for this parametric set. Both local extremes 7 and 8 exhibit similar local sensitivity and similar response for changing the r_f level, as the one depicted in figure 8 - right.

For the local extremes 7 and 8, the inverse process was restarted with discretization level $r_f = 1$. The new inverse solution was searched in vicinity of both extremes, and thus two different narrow parameter ranges were defined now – see table 6. Based on the results discussed above the specific storage was assumed to vanish from our model.

Table 6: Ranges of SHP ($\mathbf{p}_{max}$ and $\mathbf{p}_{min}$) for identifying the SHP in the top-soil layer for refinement level $r_f = 1$.

extreme	θ_s [-]	α [cm^{-1}]	n [-]	K_s [cm.hrs^{-1}]
7	0.475 - 0.712	3.042×10^{-3} - 4.562×10^{-3}	1.023 - 1.534	0.932 - 1.398
8	0.203 - 0.305	2.040×10^{-3} - 3.060×10^{-3}	1.107 - 1.661	0.895 - 1.342

18
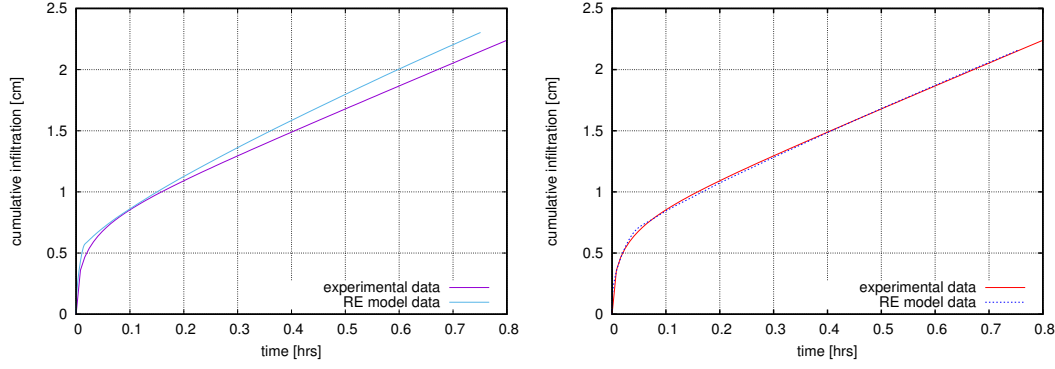
Figure 9: Left: Local extreme 7 infiltration curve for the original parameter set obtained at $r_f = 0$ and solved on model with discretization $r_f = 1$, right: solution for the updated parameter set in vicinity of the extreme 7.

359   The updated solutions maintained similar fitting qualities as the solutions obtained at $r_f = 0$, see figure 9 - right.

360   Whereas the solution depicted on figure 9 - left was created with SHP dataset obtained at previous discretization

361   level ($r_f = 0$) tested on model with increased discretization level ($r_f = 1$).

362   In order to evaluate the results obtained at $r_f = 1$ discretization level, the discretization level was increased

363   again for $r_f = 2$. New response plots were generated, an example is given in figure 4.2. For all response plots see

364   Appendix.
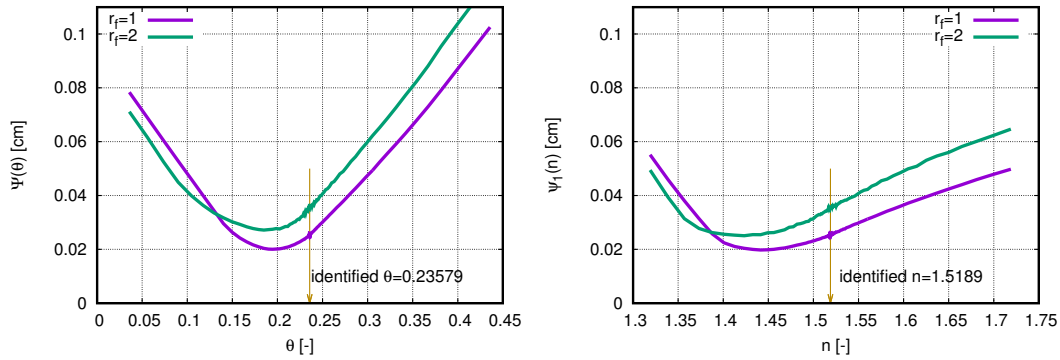
Figure 10: Response plots for $r_f = 1, 2$ for extreme 8 for parameters θ_S and n.

365   The location of peaks of the response plots for these two sequential discretization levels do not vary signifi-

366   cantly, and so no further refinements were required. The table 5 provides the final results of this inverse problem.

367   As mentioned above the solution for the extreme 6 didn't require further updates, except for the n parameter, which

368   has been slightly updated from the identified value 2.152 for new value 1.950 in accordance with the response plot

369   in figure 7 - right.

4.3. Limitations and realism of results

371   Local optima 7 resulted in the most realistic set for the podzolic top O+Ah soil layer, because of the most

372   realistic value of θ_s, which is slightly higher than for the E horizon (table 1). Table 7 shows a wide range of θ_s

373   values, which can have huge implications for the water storage of the soil. The saturated hydraulic conductivity

19

Table 7: The resulting SHP data sets.

no.	α [cm^{-1}]	n [-]	θ_s [-]	K_s [cm.hrs^{-1}]	S_s [cm^{-1}]	RMSE error (13) [cm]	
						$r_f = 1$	$r_f = 2$
6	2.580×10^{-3}	1.950	0.401	1.095	0	computed and confirmed at previous level	
7	3.229×10^{-3}	1.442	0.513	1.020	0	5.211×10^{-2}	1.217×10^{-2}
8	2.276×10^{-3}	1.519	0.236	1.036	0	2.810×10^{-2}	3.066×10^{-2}
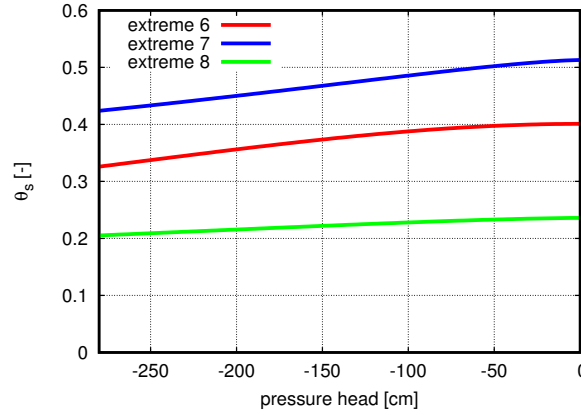
Figure 11: Resulting retention curves obtained from the inverse model.

K_s is similar across identified optima (table 7) and slightly lower than the lower horizon E (table 1). A physical explanation for the lower estimate can be that the O+Ah top layer can swell and air can be entrapped during infiltration and therefore, the volume of the effective pores can be decreased. This can be indicated by the lower values of θ_s. The identified K_s will be lower than the K_s fitted with the 1D Swartzendruber equation, because we are modeling 2D axisymmetric flow.

The identified values for α are also similar in range across the optima (table 7). α is related to the inverse of the air entry value, which in terms of suction is greater than the initial condition. Figure 11 shows that α barely impacts the shape of the retention curve in the modeled pressure head range, whereas θ_s and also n impact the retention curve significantly.

In the evaluation of the realism of the optimization we consider the treatment of the initial condition and the representativeness of the input curve as the greatest limitation. This however, does not delimit the applicability of the proposed calibration methodology.

5. Conclusions

We presented an automated calibration procedure that is able to identify optima from a relatively wide range of input parameters without convergence issues of the nonlinear operator. To solve the Richards equation we employed our open-source solver DRUtES (Kuraz et al., 2008). We also showed numerical considerations in the domain set-up of a challenging problem. We show that starting with the semi-explicit scheme can identify regions

of interest. However, the identified SHP can change dramatically with an improved numerical set-up, so that several stages of refinement are required until SHP estimates can be confirmed. We also acknowledge that for this calibration to work, the optimization algorithm needs to be able to identify multiple optima.

We applied the methodology to synthetic and real transient SR infiltration data. Our synthetic infiltration problems show that identification of soils with unimodal grain size distribution can result in multiple distinct optima with good fitting properties. Although some optima show good fits, the parameters are not necessarily physical/reasonable in the eyes of the expert. For both, the synthetic and real problems, expert knowledge on the saturated water content can aid the identification of the most reasonable optimum.

Improvements of the calibration methodology should include research on efficient numerical techniques to solve the Richards equation, such as the development of hp-adaptive approximations and adaptive domain decomposition methods.

6. Acknowledgement

References

R. Angulo-Jaramillo, J.-P. Vandervaere, S. Roulier, J.-L. Thony, J.-P. Gaudet, and M. Vauclin. Field measurement of soil surface hydraulic properties by disc and ring infiltrometers: A review and recent developments. *Soil Tillage Res.*, 55(1–2):1–29, 2000.

V. Bagarello, S. D. Prima, and M. Iovino. Estimating saturated soil hydraulic conductivity by the near steady-state phase of a beerkan infiltration test. *Geoderma*, 303(Supplement C):70 – 77, 2017.

J. Bear. *Hydraulics of groundwater*. McGraw-Hill series in water resources and environmental engineering. McGraw-Hill International Book Co., 1979.

A. Binley and K. Beven. Vadose zone flow model uncertainty as conditioned on geophysical data. *Ground Water*, 41(2):119–127, 2003.

D. Braess. *Finite elements: Theory, fast solvers, and applications in solid mechanics*. Cambridge University Press, 1997.

E. Buckingham. Studies on the movement of soil moisture. *USDA Bureau Soils – Bull.*, 38, 1907.

M. A. Celia, E. T. Bouloutas, and R. L. Zarba. A general mass-conservative numerical solution for the unsaturated flow equation. *Water Resour. Res.*, 26(7):1483–1496, 1990.

Q. Cheng, X. Chen, X. Chen, Z. Zhang, and M. Ling. Water infiltration underneath single-ring permeameters and hydraulic conductivity determination. *J. Hydrol.*, 398(1–2):135–143, 2011.

I. Christie, D. F. Griffiths, A. R. Mitchell, and O. C. Zienkiewicz. Finite element methods for second order differential equations with significant first derivatives. *Int. J. for Numer. Methods Eng.*, 10(6):1389–1396, 1976.

N. Fodor, R. Sándor, T. Orfánus, L. Lichner, and K. Rajkai. Evaluation method dependency of measured saturated hydraulic conductivity. *Geoderma*, 165(1):60–68, 2011.

O. Hrstka and A. Kucerova. Improvements of real coded genetic algorithms based on differential operators preventing premature convergence. *Adv. Eng. Softw.*, 35(3):237 – 246, 2004.

S. I. Hwang and S. E. Powers. Estimating unique soil hydraulic parameters for sandy media from multi-step outflow experiments. *Adv. Water Resour.*, 26(4):445 – 456, 2003.

A. Ibrahimbegović, C. Knopf-Lenoir, A. Kucerova, and P. Villon. Optimal design and optimal control of structures undergoing finite rotations and elastic deformations. *Int. J. for Numer. Methods Eng.*, 61(14):2428–2460, 2004.

M. Inoue, J. Šimøunek, S. Shiozawa, and J. Hopmans. Simultaneous estimation of soil hydraulic and solute transport parameters from transient infiltration experiments. *Adv. Water Resour.*, 23(7):677 – 688, 2000.

L. Jačka, J. Pavlásek, M. Jindrová, P. Bašta, M. Černý, A. Balvín, and P. Pech. Steady infiltration rates estimated for a mountain forest catchment based on the distribution of plant species. *J. For. Sci.*, 58(12):536–544, 2012.

L. Jačka, J. Pavlásek, V. Kuráž, and P. Pech. A comparison of three measuring methods for estimating the saturated hydraulic conductivity in the shallow subsurface layer of mountain podzols. *Geoderma*, 219–220(0):82 – 88, 2014.

L. Jačka, J. Pavlásek, P. Pech, and V. Kuráž. Assessment of evaluation methods using infiltration data measured in heterogeneous mountain soils. *Geoderma*, 276:74 – 83, 2016.

H. R. Kamali and S. Zand-Parsa. Optimization of a new inverse method for estimation of individual soil hydraulic parameters under field conditions. *Transactions of the ASABE*, 59(5):1257–1266, 2016.

P. Knobloch. On the choice of the supg parameter at outflow boundary layers. *Adv. Comput. Math.*, 31(4):369, Apr 2008.

J. Kohne, B. Mohanty, and J. Simunek. Inverse dual-permeability modeling of preferential water flow in a soil column and implications for field-scale solute transport. *Vadose zone journal*, 5(1):59 – 76, 2006.

J. Kool, J. Parker, and M. Van Genuchten. Determining soil hydraulic properties from one-step outflow experiments by parameter estimation. i. theory and numerical studies. *Soil Sci. Soc. Am.*, 49:1348 – 1354, 1985.

M. Kowalsky, S. Finsterle, and Y. Rubin. Estimating flow parameter distributions using ground-penetrating radar and hydrological measurements during transient flow in the vadose zone. *Adv. Water Resour.*, 27(6):583–599, JUN 2004.

A. Kucerova. *Identification of nonlinear mechanical model parameters based on softcomputing methods*. PhD thesis, Ecole Normale Supérieure de Cachan, Laboratoire de Mécanique et Technologie, 2007.

M. Kuraz and P. Mayer. Algorithms for solving darcian flow in structured porous media. *Acta Polytecnica*, 53(4):347–358, 2013.

M. Kuraz, P. Mayer, M. Lepš, and D. Trpkošová. An adaptive time discretization of the classical and the dual porosity model of Richards' equation. *J. Comput. Appl. Math.*, 233:3167–3177, 2010. ISSN: 0377-0427.

M. Kuraz, P. Mayer, and J. R. Blöcher. DRUtES – an opensource library for solving coupled nonlinear convection-diffusion-reaction equations,, 2008. Development version 2018,
http://www.drutes.org .

M. Kuraz, P. Mayer, V. Havlicek, and P. Pech. Domain decomposition adaptivity for the richards equation model. *Comput.*, 95(1):501–519, 2013a.

M. Kuraz, P. Mayer, V. Havlicek, P. Pech, and J. Pavlasek. Dual permeability variably saturated flow and contaminant transport modeling of a nuclear waste repository with capillary barrier protection. *Appl. Math. Comput.*, 219(13):7127 – 7138, 2013b.

M. Kuraz, P. Mayer, and P. Pech. Solving the nonlinear richards equation model with adaptive domain decomposition. *J. Comput. Appl. Math.*, 270:2 – 11, 2014. Fourth International Conference on Finite Element Methods in Engineering and Sciences (FEMTEC 2013).

M. Kuraz, P. Mayer, and P. Pech. Solving the nonlinear and nonstationary richards equation with two-level adaptive domain decomposition (dd-adaptivity). *Appl. Math. Comput.*, 267:207 – 222, 2015.

L. Lassabatère, R. Angulo-Jaramillo, J. M. Soria Ugalde, R. Cuenca, I. Braud, and R. Haverkamp. Beerkan estimation of soil transfer parameters through infiltration experiments–best. *Soil Sci. Soc. Am. J.*, 70(7):521 – 532, 2006.

M. Leps. Parallel multi-objective identification of material parameters for concrete. In *Proceedings of the Ninth International Conference on*

the *Application of Artificial Intelligence to Civil, Structural and Environmental Engineering, Stirling: Civil-Comp Press Ltd*, 2007.

S. Mous. Identification of the movement of water in unsaturated soils: the problem of identifiability of the model. *J. Hydrol.*, 143(1):153 – 167, 1993. XVI General Assembly of the European Geophysical Society.

M. Nakhaei and V. Amiri. Estimating the unsaturated soil hydraulic properties from a redistribution experiment: Application to synthetic data. *J. Porous Media*, 18(7):717–729, 2015.

C. Peña-Sancho, T. Ghezzehei, B. Latorre, C. González-Cebollada, and D. Moret-Fernández. Upward infiltration–evaporation method to estimate soil hydraulic properties. *Hydrol. Sci. J.*, 62(10):1683–1693, 2017.

W. D. Reynolds. *Saturated hydraulic properties: Ring infiltrometer, in: Carter M.R., Gregorich, E.G. [Eds.], Soil Sampling and Methods of Analysis, 2nd ed*. CRC Press Taylor & Francis, Boca Raton, USA, pp. 1043–1056, 2008a.

W. D. Reynolds. *Saturated hydraulic properties: Well permeameter, in: Carter M.R., Gregorich, E.G. [Eds.], Soil Sampling and Methods of Analysis, 2nd ed*. CRC Press Taylor & Francis, Boca Raton, USA, pp. 1025–1042, 2008b.

L. A. Richards. Capillary conduction of liquids through porous mediums. *J. Appl. Phys.*, 1(5):318–333, 1931.

G. Roos, H., M. Stynes, and L. Tobiska. *Numerical Methods for Singularly Perturbed Differential Equations, Convection-Diffusion and Flow Problems*. Springer-Verlag Berlin Heidelberg, 1996.

A. Saltelli, K. Chan, and E. Scott. *Sensitivity Analysis*. Wiley series in probabillity analysis. John Wiley & Sons, 2000.

M. G. Schaap, F. J. Leij, and M. T. van Genuchten. rosetta: a computer program for estimating soil hydraulic parameters with hierarchical pedotransfer functions. *J. Hydrol.*, 251(3–4):163 – 176, 2001.

D. Swartzendruber. A Quasi-Solution of Richards Equation for the Downward Infiltration of Water into Soil. *Water Resour. Res.*, 23(5): 809–817, MAY 1987.

M. T. van Genuchten, J. Simunek, F. J. Leiji, and M. Sejna. RETC, version 6.02 – code for quantifying the hydraulic functions of unsaturated soils., 2009.

M. van Genuchten. Closed-form equation for predicting the hydraulic conductivity of unsaturated soils. *Soil Sci. Soc. Am. J.*, 44(5):892–898, 1980.

Z. Vitingerova. *Evolutionary Algorithms for Multi-Objective Parameter Estimation*. PhD thesis, CTU in Prague, Fac. of Civil Eng., 2010.

X. Xu, C. Lewis, W. Liu, J. Albertson, and G. Kiely. Analysis of single-ring infiltrometer data for soil hydraulic properties estimation: Comparison of best and wu methods. *Agric. Water Manag.*, 107(Supplement C):34 – 41, 2012.

A. Younes, T. Mara, M. Fahs, O. Grunberger, and P. Ackerer. Hydraulic and transport parameter assessment using column infiltration experiments. *Hydrol. Earth Syst. Sci.*, 21(5):2263–2275, 2017.

Z.-Y. Zou, M. Young, Z. Li, and P. Wierenga. Estimation of depth averaged unsaturated soil hydraulic properties from infiltration experiments. *J. Hydrol.*, 242(1–2):26 – 42, 2001.

Appendix A. Sensitivity analyses

The first procedure, which is typically required before proceeding the inverse modeling procedures, is the global sensitivity analyses on selected parameter ranges, see table 2. For simplicity the sensitivity analyses was conducted just for the first objective function (13). This strategy is in line with the statements given in the last paragraph of the section 2.4.1. In total 10.000 samples of the objective function (13) were evaluated, in order to obtain the Total Sobol Index for each parameter (Saltelli et al., 2000). The values of the Total Sobol Indices are given in table A.8. Since the evaluated Total Sobol Index for each parameter was nearly 0.9, our model exhibits an excellent sensitivity for all SHP parameters.

Table A.8: Total Sobol indices for the searched SHP parameters.

parameter	α	n	K_s	θ_s	S_s
Total Sobol Index	0.850	0.921	0.876	0.868	0.884

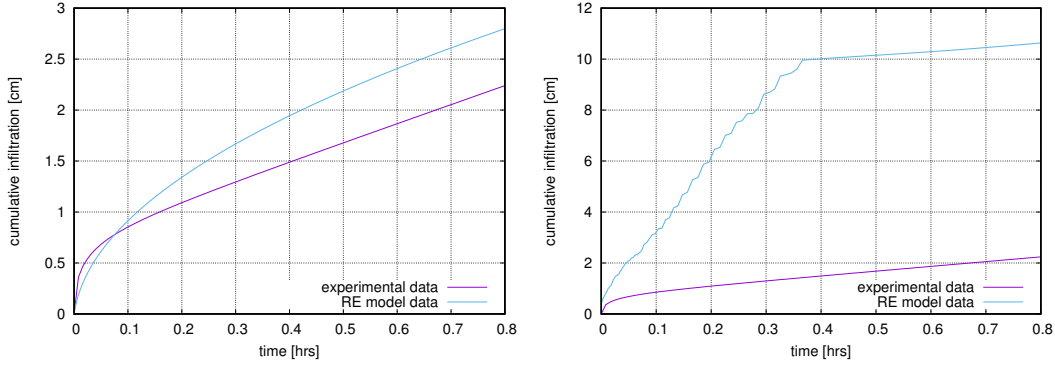# Appendix B. Solutions after the first identification run with $r_f = 0$ and $r_f = 1$.

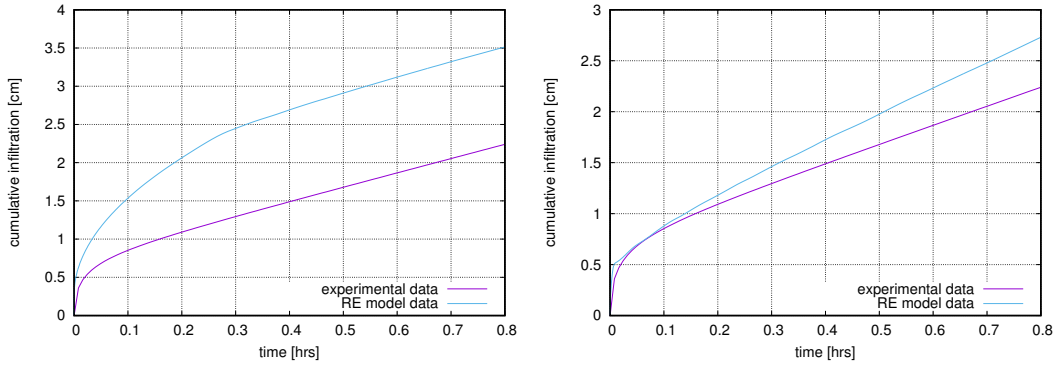Figure B.12: Refinement level $r_f = 0$: Local extreme 1 , Right: Local extreme 2.

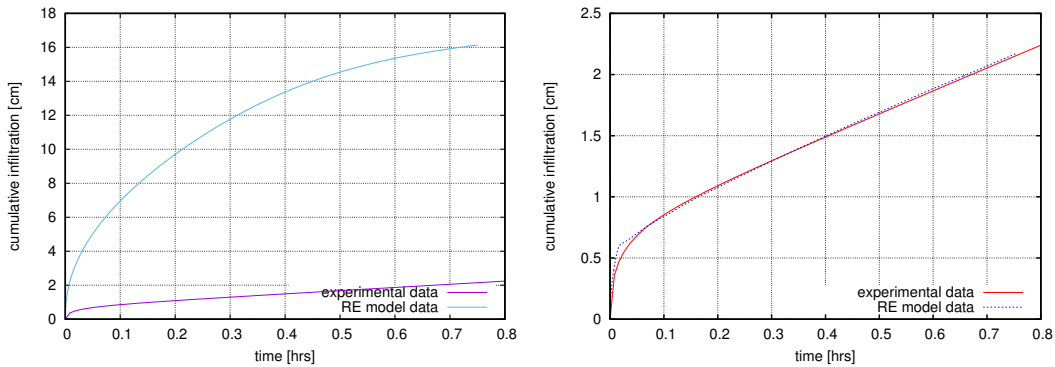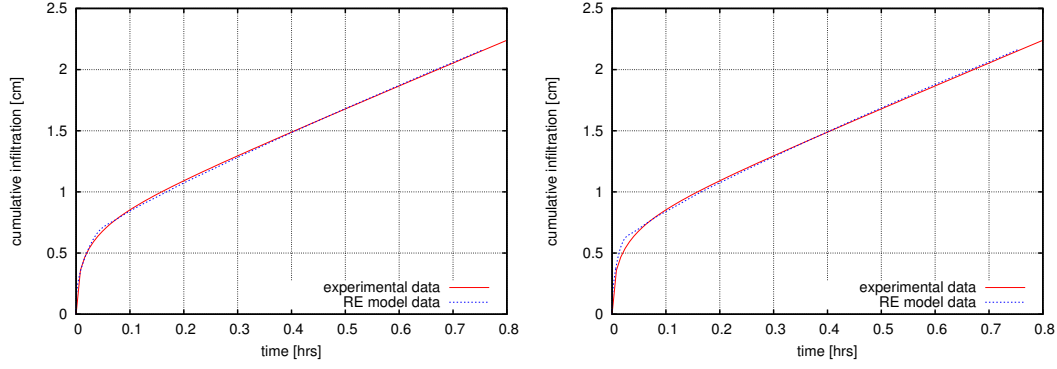Figure B.13: Refinement level $r_f = 0$: Local extreme 3 , Right: Local extreme 4.

Figure B.14: Refinement level $r_f = 0$: Local extreme 5 , Right: Local extreme 6.

Figure B.15: Refinement level $r_f = 0$: Local extreme 7 , Right: Local extreme 8.

Appendix C. Response plots for objective functions, $r_f = 0, 1$

Response plots of the objective functions for the local extreme 6 are depicted in figures Appendix C – Appendix C.
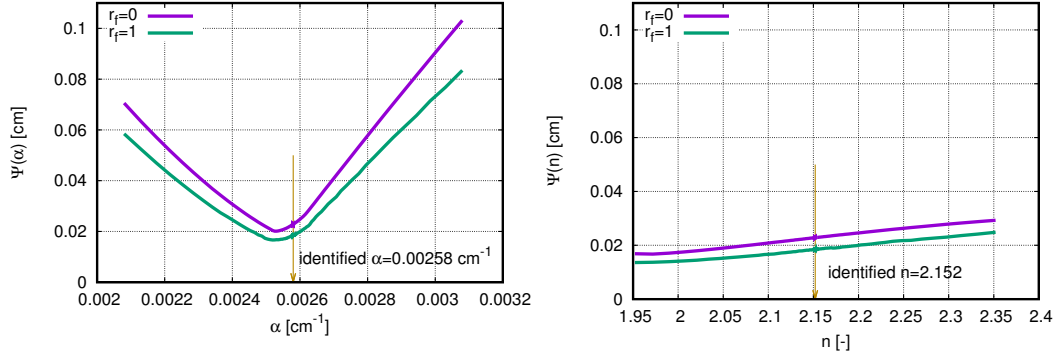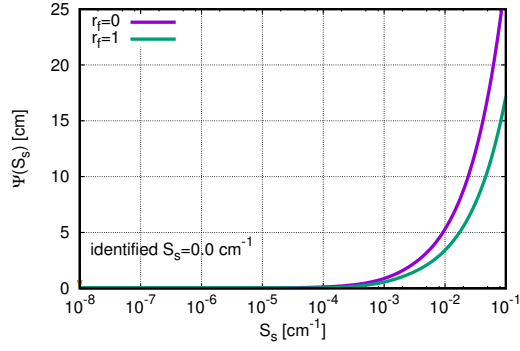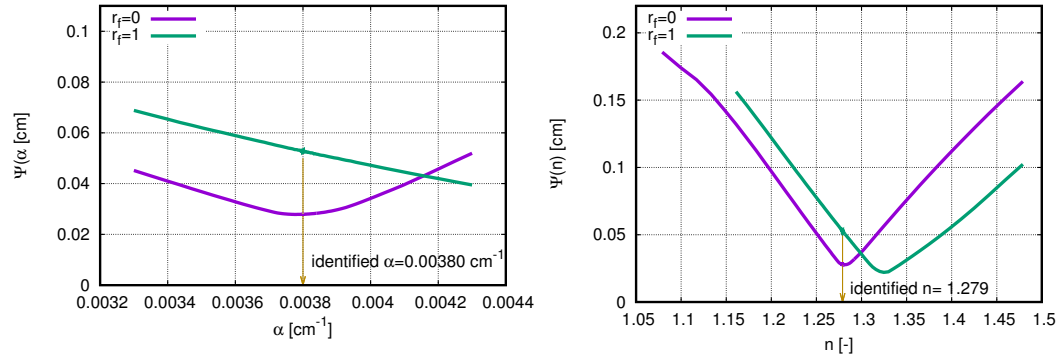

Figure C.16: Response plots for $r_f = 0, 1$ for extreme 6 for parameters α and n.
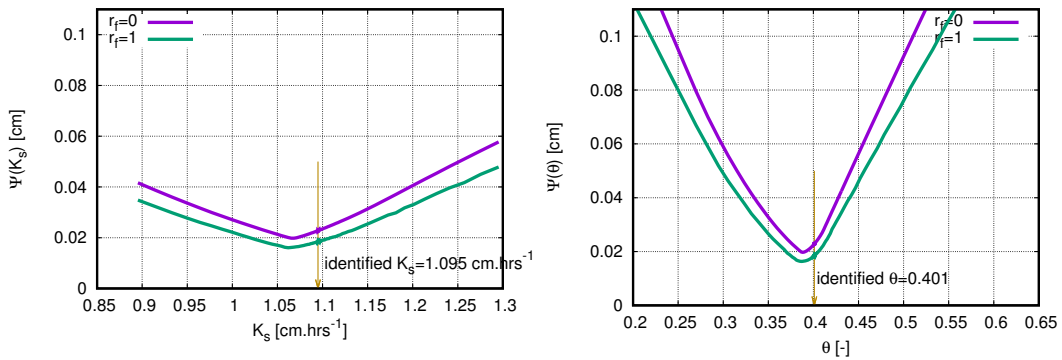
Figure C.17: Response plots for $r_f = 0, 1$ for extreme 6 for parameters K_s and θ_s.

Response plots of the objective functions for the local extreme 7 are depicted in figures Appendix C – Appendix C.

Response plots of the objective functions for the local extreme 8 are depicted in figures Appendix C – Appendix C.

25
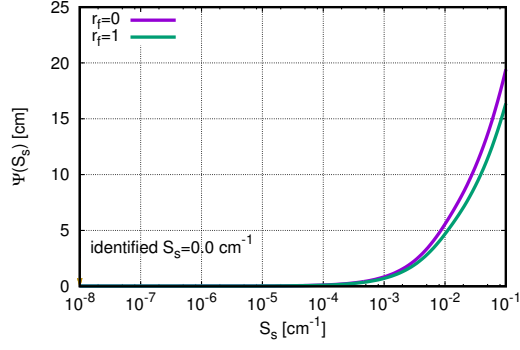
Figure C.18: Response plots for $r_f = 0, 1$ for extreme 6 for parameter S_s
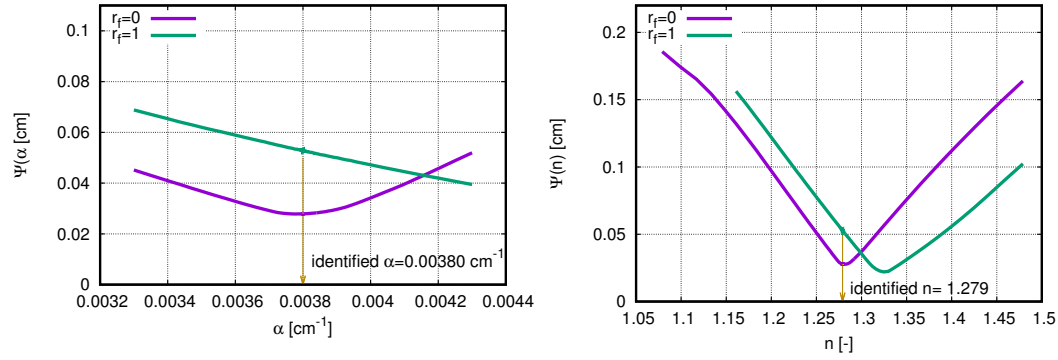
Figure C.19: Response plots for $r_f = 0, 1$ for extreme 7 for parameters α and n.
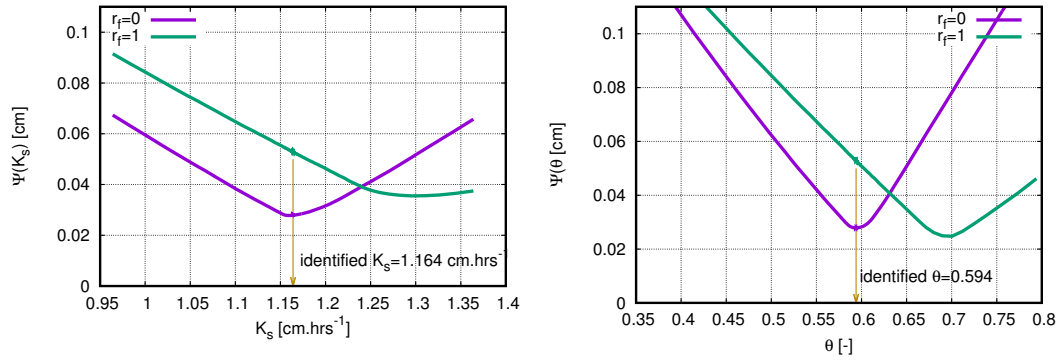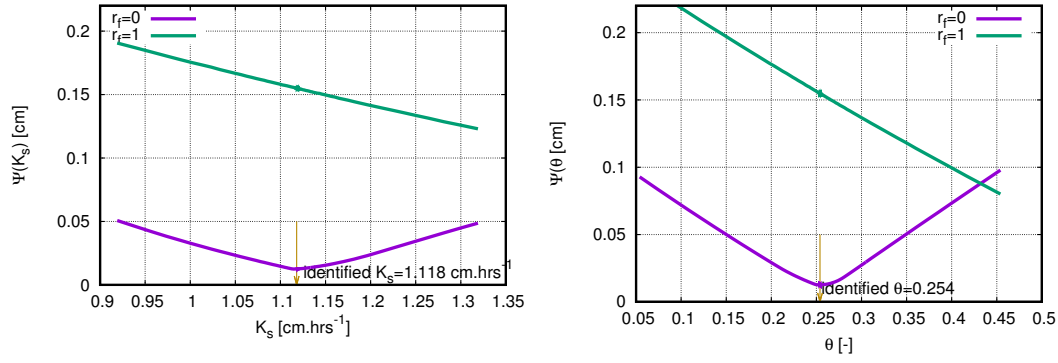

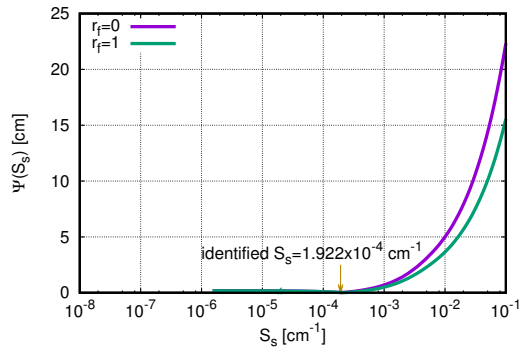Figure C.20: Response plots for $r_f = 0, 1$ for extreme 7 for parameters K_s and θ_s.

Appendix D. New solutions for $r_f = 1$

The updated solutions for the local extremes 7 and 8 are depicted in figures Appendix D and Appendix D.

Appendix E. Response plots for objective functions, $r_f = 1, 2$

Response plots of the objective functions for the updated local extreme 7 for $r_f = 1, 2$ is depicted in figures Appendix E - Appendix E.

Figure C.21: Response plots for $r_f = 0, 1$ for extreme 7 for parameter S_s

Figure C.22: Response plots for $r_f = 0, 1$ for extreme 8 for parameters α and n.

Figure C.23: Response plots for $r_f = 0, 1$ for extreme 8 for parameters K_s and θ_s.

Figure C.24: Response plots for $r_f = 0, 1$ for extreme 8 for parameter S_s.
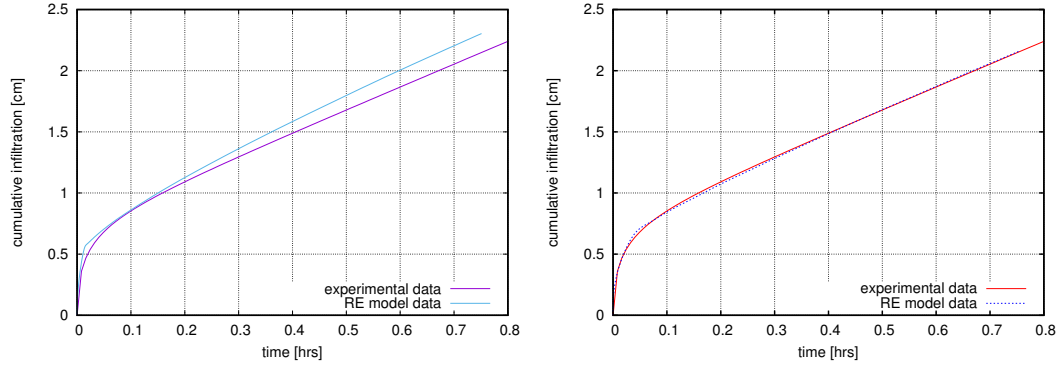
Figure D.25: Left: Local extreme 7 infiltration curve for the original parameter set obtained at $r_f = 0$ and solved on model with discretization $r_f = 1$, right: solution for the updated parameter set in vicinity of the extreme 7.
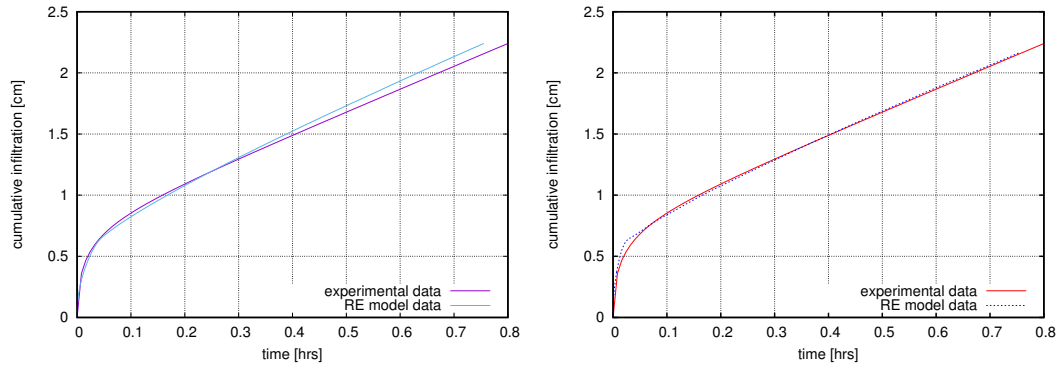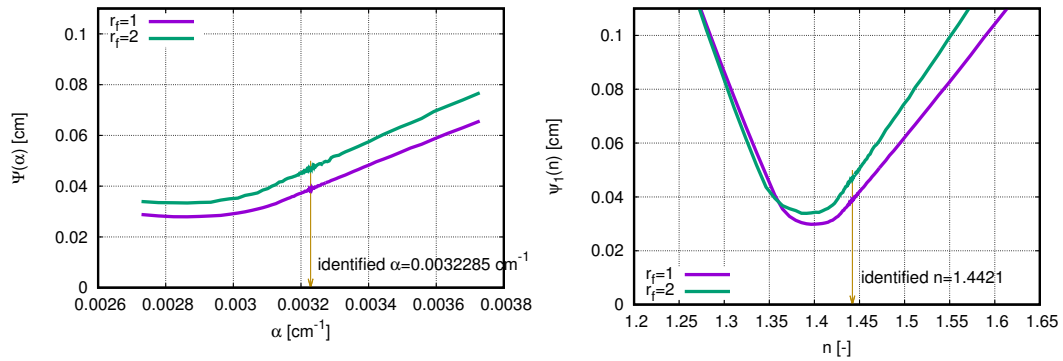

Figure D.26: Left: Local extreme 8 infiltration curve for the original parameter set obtained at $r_f = 0$ and solved on model with discretization $r_f = 1$, right: solution for the updated parameter set in vicinity of the extreme 7.

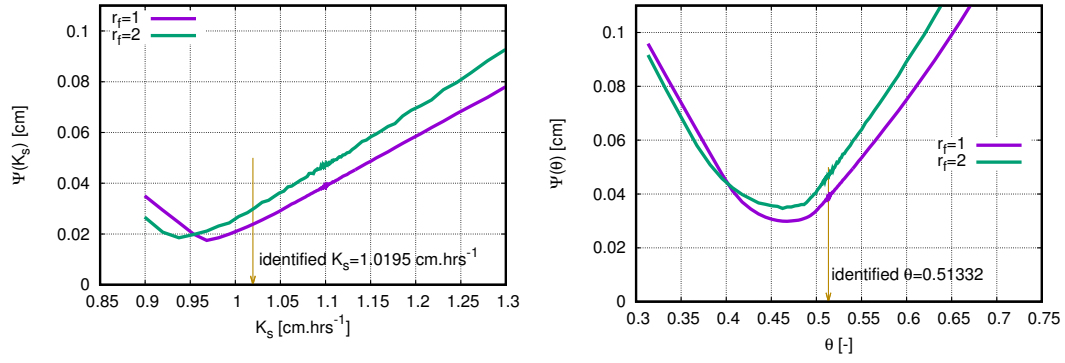Figure E.27: Response plots for $r_f = 1, 2$ for extreme 7 for parameters α and n.

Figure E.28: Response plots for $r_f = 1, 2$ for extreme 7 for parameters K_s and θ_s.
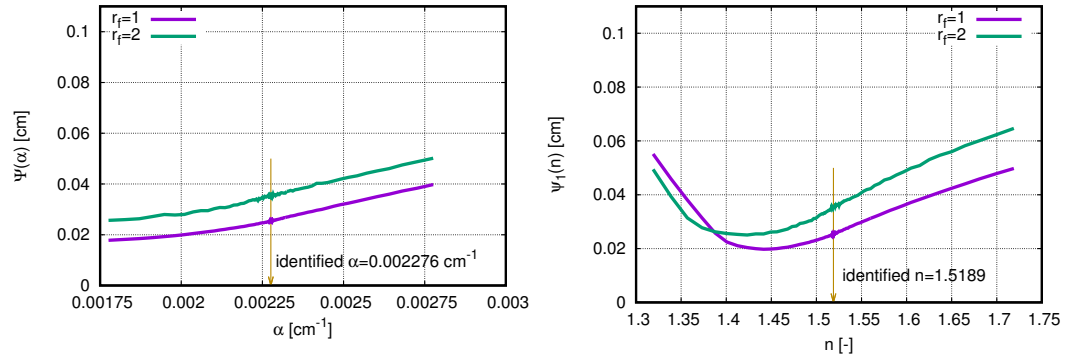

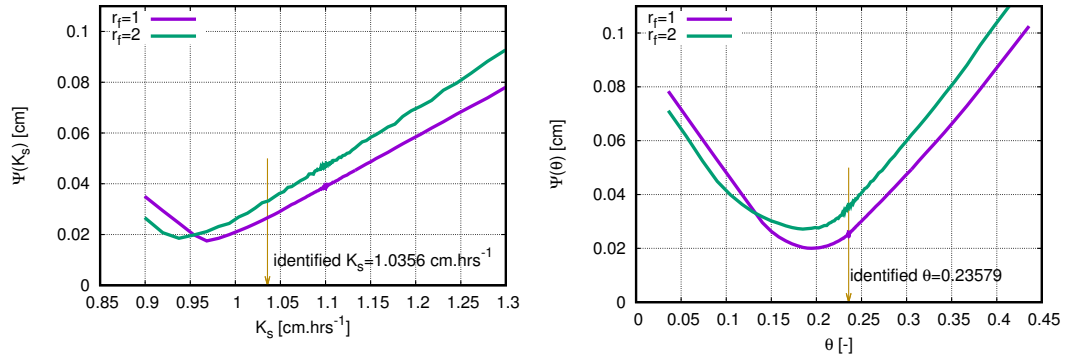Figure E.29: Response plots for $r_f = 1, 2$ for extreme 8 for parameters α and n.

Figure E.30: Response plots for $r_f = 1, 2$ for extreme 8 for parameters K_s and θ_s.